

14 November, 1996

An All-Solid State Central Tracker for the Proposed DESY Electron-Positron Linear Collider

B. J. King

DESY

F-OPAL

Notkestrasse 85

22607 Hamburg

Deutschland

email: KING@OPL01.DESY.DE

Abstract

This report describes an all-solid state central tracker which is intended for use in a detector at the proposed DESY 500 GeV electron-positron linear collider or a similar accelerator. The precise position measurements from position-sensitive silicon detectors give the tracker an outstanding momentum resolution for high momentum tracks: $\sigma_p/p^2 = 3.6 \times 10^{-5} (\text{GeV}/c)^{-1}$ for tracks perpendicular to the beam-line. The report concludes with an example layout for a detector which uses this central tracker.

1 Introduction

Rapid progress in solid-state detector technology has made large area solid-state central trackers an attractive option for collider experiments. Examples are the CMS [1, 15] and ATLAS [2, 16] experiments at the LHC, the latter of which will use 42 m² of microstrip detectors and approximately 4 m² of pixel detectors in its central tracker.

This report describes an all-silicon central tracker (CT) which is intended for use at a TeV-scale electron-positron linear collider, and which features an outstanding momentum resolution of $3.6 \times 10^{-5} (\text{GeV}/c)^{-1}$ for high momentum tracks perpendicular to the beam-line.

A cross-section of the CT is displayed in figure 1, and figure 2 gives a 3-dimensional cut-away view. Silicon position-sensitive detectors are arranged in 10 concentric ellipsoidal shells around the interaction point (IP): pixel detectors in the 6 innermost layers and microstrip detectors in the 4 large outer layers. The outer radius of the tracker is 1.00 m, the half-length is 1.70 m and the CT covers 99.3 percent of the solid angle. The minimum polar angle, 120 milliradians, coincides with the outer edge of the tungsten radiation mask. The ellipsoidal geometry can easily accommodate tracking coverage down to even smaller polar angles, if it is found that the tungsten mask can be reduced in size.

The 6 innermost shells comprise 1.75 square metres of silicon pixel detectors while the 3 shells at mid-radius use back-to-back silicon microstrip detectors in stereo geometry and the outermost shell uses a triple layer of microstrips in “U-V-X” geometry. The total area of strip detectors is 96 square metres.

Details of the tracker layout are given in section 2 and the silicon detectors

are discussed in section 3. Sections 4, 5 and 6 address the technical issues of pattern recognition, mechanical support structure and mechanical services, and the alignment of the silicon wafers, respectively. The performance of the tracker for vertexing and momentum resolution is discussed in section 7, and the cost of the tracker in section 8. Finally, an example design for the entire detector is presented in section 9.

The central tracker and detector designs have been specifically geared towards the two linear collider options which have been proposed for the DESY Laboratory. In this report, the two options will be referred to as “TESLA” and “S-band”, and the generic linear collider as the “TLC” (“TeV-scale linear collider”). The central tracker design will often be abbreviated to “CT” and the overall detector design as “TLD” (“detector for a TeV-scale linear collider”).

2 Layout of Central Tracker

The main design goals for the layout of the CT have been to provide excellent vertexing and nearly optimal momentum resolution for high-momentum tracks, consistent with robust pattern recognition and convenient mechanical layout. Of necessity, there is some level of compromise between the competing design issues. For example, the mid-radius region of the tracker is the most critical for determining the sagitta of high-momentum tracks. However, material in this region degrades the measurement of low-momentum tracks. The demands of pattern recognition and mechanical support also favour spreading out the shells rather than concentrating them at mid-radius.

The use of many small solid-state detectors, as opposed to a gas-based

tracking chamber, introduces a much greater freedom in the choice of tracker layout. The ellipsoidal shell geometry which was chosen for the CT has several attractive features relative to, say, a barrel-plus-endcap geometry:

- all of the ellipsoidal surface is reasonably projective to the interaction point (IP). The silicon wafers can be made projective with little additional tilting.
- the explicit radial ordering of the shells is helpful for pattern recognition. (See section 4.)
- the regions between the shells are available for a stiff, light 3-dimensional mechanical support structure and also provide natural outlets for routing cables and cooling pipes. (See section 5.)
- tracking coverage can be provided down to small polar angles with no barrel-to-endcap cross-over region and with a smooth dependence of the resolution functions on polar angle.
- the smaller outer surface area of the tracker can be surrounded by a cheaper, more projective electromagnetic calorimeter than would be the case with, say, a cylindrical geometry. (See section 9.)

Partly because of these advantages, the ellipsoidal geometry has already been chosen for the tracking spectrometer of the CLAS detector at CEBAF [4] (using curved drift chambers) and the BaBar silicon vertex tracker [5] at the PEP-II asymmetric electron-positron collider at SLAC.

Pixel detectors (either CCD's or APS's – see the following section) are strongly preferred over microstrips for pattern recognition in the 6 innermost layers, where beamstrahlung electrons will produce of order 1000 hits – see

section 4. In contrast, the hit multiplicities in the 4 large outer shells are dominated by the physics event itself, giving only of order 100 hits spread over areas of a square meter or more. Stereo layers of microstrips (or a triple layer, in the case of the outermost shell) give adequate granularity for these shells at an affordable price.

The strip detectors are tilted to make an angle which is projective to the interaction point (IP). Projective detectors give the optimal point resolution for stiff tracks, and this geometry also covers the CT acceptance using the smallest possible area of detectors, saving in cost and material budget.

The wafers overlap in both the polar and azimuthal views, as viewed from the IP, which makes the CT hermetic to tracks originating near the IP. In fact, the CT is also hermetic to soft tracks from the IP, since their transverse momentum is initially in the radial direction and the track's polar angle decreases (for forward-going tracks) as the track spirals and the radial momentum component is transferred into the azimuthal component. Thus, these dipping tracks see even more overlap in the wafers than stiff tracks. The hermeticity of the CT has been checked in Monte Carlo-based track simulations.

The 6 pixel layers near the interaction point (IP) are the most important for finding decay vertices from beauty and charm hadrons and tau leptons. For this reason, they will sometimes be referred to as the “vertexing layers” or, collectively, as the “vertex detector”. However, it should be remembered that, as with the other tasks of the CT, information from the entire tracker is used for vertex finding.

The layout of the vertexing layers is similar to that of the BaBar silicon vertex tracker [5]. The innermost layer, at a radius of 2 cm, is a cylinder, but

the remaining 5 concentric layers consist of a central cylinder with end-cap cones at each end. Two additional end-caps at each end of the vertex detector ensure 6 layers of vertexing for all tracks down to the minimum polar angle of the tracker acceptance, at 120 mrad from the beam direction.

The barrel regions of the 6 layers have radii of 2, 4, 7, 10, 13 and 16 cm. The innermost vertexing layer is placed directly outside the beam-pipe to minimize the extrapolation distance to decay vertices. The 2 cm radius of this layer is well matched to the decay lengths of relativistically boosted beauty and charm hadrons – about 1 cm for energies of 100 GeV – while avoiding the rapidly increasing backgrounds at smaller radii.

The nearly-spherical geometry of the vertex detector means that the wafers are all fairly projective to the IP, giving nearly optimal point resolutions for almost all tracks. This geometry is particularly appropriate for electron-positron colliders, as opposed to e-p or p-p colliders, since electron-positron colliders have a beam spot which is very small compared to the scale of the detector wafers. Also, the energies and, hence, lifetime distributions of beauty, charm and tau particles don't depend strongly on the polar angle.

The CT is elongated along the direction of the magnetic field (i.e. parallel to the beam axis) to improve the momentum resolution for forward-going tracks. The benefits of elongating the CT must be weighed against the disadvantages for the tracker and the sub-detectors outside it, such as a more expensive, less projective electromagnetic calorimeter and a longer magnet.

Typically, trackers at electron-positron colliders are less elongated than their counterparts at e-p and p-p colliders, where the interesting physics processes are more concentrated at small angles to the beam direction. This reflects the hard, point-like nature of electron-positron collisions relative to

the softer interactions of composite protons. Following this expectation, the central region of the detector is found to be relatively important for the physics processes that have been studied so far for the TLC [6].

For the chosen aspect ratio of the tracker, eighty-seven percent of the CT's solid angle has a momentum resolution within a factor of two of that perpendicular to the beam-line. This is similar to, or slightly greater than, the corresponding percentage for today's trackers at high energy electron-positron colliders. Even at the minimum polar angle of the CT acceptance, at 120 mrad from the beam-line, the momentum resolution is still sufficient to determine the charge of tracks up to the beam energy. (See section 7 for details on the angular dependence of the momentum distribution.)

The stereo layers of microstrips which instrument the 4 large tracker shells consist of tiles containing two back-to-back single-sided silicon detectors, for reasons discussed in the next section. For optimal resolution of tracks' bend coordinate, all of the tiles are oriented so that the stereo strip directions are bisected by a plane containing the beam-line axis. In addition, the tiles in the outermost shell incorporate a third single-sided detector whose strips are oriented in this plane, bisecting the stereo directions. This "U-V-X" geometry gives the redundancy of 3 position measurements with the full lever-arm of the tracker.

The main motivation for using stereo strips is that the two hits produced by a track can immediately be combined into a space point as the first step of a pattern recognition algorithm – see section 4. In this respect, the stereo configuration also has important advantages over back-to-back orthogonal strips, since hit ambiguities ("ghost hits") will usually only occur when a second track crosses the wafer within a defined area of order (stereo angle)–

times–(strip length) around the first, which will correspond to only a small fraction of the wafer area. In addition, the smaller overlap area reduces the chance that a random noise hit will be added on to a track hit to contribute a ghost hit, and it will also be uncommon for two random noise hits to occur close enough together to be paired into a space point. This means that most random noise hits will be rejected when space points are constructed as the first step of the pattern recognition algorithm.

Although stereo strips give a position resolution perpendicular to tracks' bend coordinate which is only moderate, the physically important bend coordinate resolution – which determines the momentum measurement – is essentially as good as if the two planes of strips had been placed completely perpendicular to the bend coordinate. This behaviour can be derived as follows.

Consider strips with gaussian resolution σ which are oriented at (small) stereo half-angles α to the z-axis, in a local coordinate system with the wafer in the x-z plane. Using polar coordinates, $\rho = x^2 + z^2$ and $\theta = \tan^{-1}(\frac{x}{z})$, one can write the following formula for the negative log likelihood distribution, $-L$, of the true position of a hit which is measured to be at the origin:

$$\begin{aligned}
 -L &= \left(\frac{\rho}{\sigma}\right)^2 \{\sin^2(\theta - \alpha) + \sin^2(\theta + \alpha)\} \\
 &= 2\left(\frac{\rho}{\sigma}\right)^2 \{\sin^2 \theta \cos^2 \alpha + \cos^2 \theta \sin^2 \alpha\} \\
 &\simeq \frac{2(1 - \alpha^2)}{\sigma^2} x^2 + \frac{2\alpha^2}{\sigma^2} z^2,
 \end{aligned}$$

where terms of order α^4 and higher have been neglected in the final step of the derivation. The likelihood function is seen to have an elliptical distri-

bution with the major axis along the z direction, corresponding to Gaussian resolutions of $\sigma(1 - \frac{\alpha^2}{2})/\sqrt{2}$ and $\sigma/(\sqrt{2}\alpha)$ for the x and z views, respectively. Since $\alpha \ll 1$, the resolution in the x view is very close to the optimal value, $\sigma/\sqrt{2}$, which would be obtained if both layers of strips were oriented parallel to the z-axis.

From the above discussion, the choice of stereo angle can be seen to be a trade-off between simpler pattern recognition and degraded resolution in the z coordinate. In principle, the pattern recognition capabilities of the tracker can be optimized by using different stereo angles in different regions of the tracker. For example, smaller stereo angles could be used in the forward regions of the mid-radius shells, where the track density is greater than in the central region. In general, a reasonable choice for stereo angle might be similar to the 2 degree angle which will be used for the tracker upgrade of the D0 detector at the Fermilab Tevatron [19].

3 Silicon Microstrip and Pixel Detectors

This section presents general comments on the likely design parameters for the silicon microstrip and pixel detectors, beginning with a discussion on the microstrip detectors.

The design of the silicon microstrip detectors can draw on experience from many successful vertex detectors in today's collider experiments, some of which have had design constraints at least as demanding as will be imposed at the TLC. For the microstrip detectors, the only new feature for the CT is the logistics challenge of maintaining quality control over a larger surface area of detectors than exists today.

In spite of the large surface area of microstrips, it should be noted that the approximately 2×10^7 channels of microstrips is still considerably less than the of order 10^8 channels of pixels required for the vertex detector. The VXD3 vertex detector [8], which has just begun taking data in the SLD collider detector, already incorporates 3×10^8 channels of CCD pixels. (To get a feel for the numbers, 2×10^7 microstrip channels corresponds to 100 m^2 of 10 cm long microstrips with a 50 micron readout pitch, while 1 m^2 of $100\mu\text{m} \times 100\mu\text{m}$ pixels is 10^8 channels.) Both the microstrip and pixel detectors will incorporate front-end readout chips to sparsify (via zero suppression), multiplex and buffer the channel signals, thus reducing the output load to a more manageable level for the downstream electronics [1, 2].

For the best possible performance, it is likely that the silicon microstrip detectors and much of the associated electronics would be custom-designed for this tracker. This is relatively normal for collider detectors – taking advantage of some of the techniques and facilities used for commercial silicon chip design – and is certainly justified by the large wafer area required for this tracker.

Many of the design parameters of microstrip detectors have become relatively standardized. A wafer thickness of 300 microns is the norm, and a minimum strip read-out pitch of 50 microns is fixed by the size of today’s front end electronics. A strip pitch of 25 microns is often used, with the “floating strips” between the read-out strips used to collect charge by capacitive coupling to the adjacent read-out strips. This technique gives an improved interpolation of track positions when combined with charge weighting of the signals on the read-out strips. High momentum tracks will pass through the wafers at near normal incidence and, for such tracks, point resolutions of

about 8 microns are typical for experiments using this configuration. The length of the wafers will be determined by a compromise between reducing the number of electronics channels and the degradation of readout signal-to-noise due to increasing strip capacitance. Strip lengths from 6 to 12 cm have become fairly common, and the BaBar silicon vertex tracker [5] intends to use strips as long as 24 cm.

Conventionally, single-sided silicon detectors have read out the positively-charged “holes” produced by the ionizing track, rather than the ionization electrons. In a 4 Tesla magnetic field, the holes drift through the silicon at a 7 degree Lorentz angle to the electric field direction. Although this is probably not serious anyway, it can be corrected for by tilting the detectors slightly in the azimuthal direction.

The magnetic field poses much more serious problems for double-sided read-out schemes, where the ionization electrons are also read out from the back surface of the wafer. Electrons experience a much larger Lorentz angle than holes – 33 degrees at 4 Tesla – due to their greater mobility. The detectors cannot be tilted to simultaneously satisfy the Lorentz angles of both holes and electrons, and this level of transverse drift might be expected to introduce resolution tails and somewhat degrade the measurement of charged tracks at normal incidence to the wafer. Double-sided detectors are also more difficult and expensive to manufacture, currently costing about three times as much as single-sided detectors.

These disadvantages suggest that back-to-back single-sided wafers are to be preferred for the CT’s stereo layers, despite the additional material this introduces: one extra wafer thickness, which is 300 microns or 0.3 percent of a radiation length.

Given the size of the CT, it is likely that the front-end electronics would be mounted on the wafers, as opposed to carrying the raw signals out of the tracker on flexible fanout circuits. Several types of existing front-end chips, typically with 64 or 128 readout channels per chip, already offer a variety of attractive read-out options for the CT [3]. To reduce the rate of data flow, front-end chips can store the amplified signals from each strip in an analogue pipeline, to be read out only on the receipt of a level-one event trigger. Both analogue and digital read-out options are available, using either electrical or optical links. Dedicated fast trigger channels can also be included, perhaps with coarser granularity.

Regarding the time constraints on the electronics, the TESLA design's 707 ns beam-crossing interval places only relatively moderate demands on the read-out electronics for the silicon strips, but the 6 ns interval for S-band is approaching the smallest interval at colliders planned for the near future [11]: 2 ns for the KEK B factory. For this option, the read-out would probably have to integrate over a few beam crossings.

The main cause of radiation damage to the detector wafers will be neutrons of energies around 1 MeV [7], mostly originating from the area of the final focus magnets. The vertexing layers will be exposed to of order 3×10^9 neutrons per square centimetre per year of operation [7] (within large uncertainties), and the silicon strips to less than this. This is considerable, but, for comparison, is still 4 orders of magnitude below the dose rate expected at the LHC vertex detectors.

In general, the read-out electronics can be made more robust against radiation damage than the substrate itself [8], and it can even be designed to compensate for radiation-induced changes in the signal from the silicon [1, 2].

Radiation-hard electronics will be required for the CT, but won't have to cope with the level of bulk damage to the silicon substrate that is expected for the detectors at the LHC and that imposes stringent requirements on the LHC electronics. There is also no strong motivation to use a material other than silicon as the detector substrate.

In short, the technology for silicon strip detectors is already well established, and the detector design for the TLC will be geared towards optimizing the resolution and reliability of the detectors.

In contrast to the established pedigree for microstrips, there are no pixel detectors in operation today that satisfy all of the performance requirements of the CT vertex detector. However, rapid progress is being made in this field and it is a reasonable extrapolation to assume that such devices will become available within the next couple of years.

Pixel detectors come in two varieties: charge coupled devices (CCD's) and active pixel sensors (APS's). (See reference [8] for detailed descriptions of both pixel detectors and microstrip detectors.) Each of the two types has advantages and disadvantages. CCD's can be made thinner and with smaller pixels, giving them an important advantage over APS's in position resolution. CCD's using 20 micron x 20 micron pixels can achieve outstanding point resolutions of 3.5 microns [9], while APS's might have trouble coming within a factor of two of this figure.

CCD's are also cheaper than APS's, and have the advantage of several years of successful data-taking experience with the VXD2 and VXD3 vertex detectors in the SLD experiment. To balance this, APS's have already been successfully used in a fixed target experiment at CERN and have now begun data-taking in the forward region of the DELPHI vertex detector. Also, a

vigorous research and development program for APS's is being carried out for the ATLAS [2] and CMS [1] vertex detectors at the LHC, both of which will have similar areas to the CT vertex detector and must meet much more stringent design demands.

The Achilles's heel of CCD's is their intrinsically slow read-out. For both the TESLA and S-band accelerator options, the CCD's would unavoidably collect background hits from some few tens of beam crossings around the triggered event. Also, some amount of dead-time (less than 30%) might be introduced for CCD's with the TESLA option. (See [9] for CCD read-out strategies at the FLC.) CCD's are also more vulnerable to radiation damage than either APS's or microstrips. The expected neutron background at the TLC is right at the limit of what is tolerable for today's CCD detectors.

In summary, many attractive design options already exist for the silicon microstrip detectors, while the contrasting advantages of CCD's and APS's and the rapid advances in both technologies suggest that it would be sensible to delay the choice of pixel technology for as long as is practical.

4 Pattern Recognition

The task of doing track-finding using a few widely spaced, precise coordinate measurements is familiar at test-beam lines and fixed target experiments but relatively new for colliders. This section describes some simple studies which give confidence in the pattern recognition performance of the CT.

The CT measures space points in 10 concentric layers plus one additional sampling at the outermost layer, giving 11-plus-10 samplings in/out of the bend plane. Of other trackers at existing and proposed collider experiments,

CMS [1] has the most similar pattern recognition strategy, with approximately 12-plus-6 or 12-plus-7 samplings (depending on the track direction). It should be noted that the pattern recognition task is expected to be much more demanding for CMS than for the CT, with a hit density expected to be larger by up to two orders of magnitude and with lower detector efficiencies due to radiation damage. In both tracker designs the enormous number of channels – of order 10^8 pixel channels and 10^7 microstrip channels – would be expected to be well suited for reconstructing high multiplicity events.

Another sparse-sampling tracker design for a collider experiment is the BaBar silicon vertex tracker [5], which is intended to perform stand-alone tracking of low momentum tracks. The BaBar design has only 5-plus-5 samplings in/out of the bend plane, reflecting the less dense track environment at the lower energy PEP-II electron-positron collider.

From the above discussion, the CT design appears to be more conservative and robust for its pattern recognition task than either the CMS or BaBar trackers. To check this assertion, a simple track-finding software package was developed and tested on Monte Carlo-generated events to give a more quantitative assessment of the the pattern recognition performance of the CT [10].

The algorithm searches for track “3-seeds” consisting of triplets of space points in any 3 distinct detector shells, where the space points come either from pixel hits or from matched pairs of hits in the double layers of stereo microstrips. Unmatched hits in the silicon microstrips are simply ignored – which is obviously not optimal. Pairs of 3-seeds with 2 space points in common are then merged and tested to see if the 4 space points form a new, larger track seed (a “4-seed”). Complete track candidates are grown by

continuing this process of seed-merging.

The algorithm was tested on a previous design iteration of the CT which incorporated only 8 shells, as opposed to the 10 shells of the current version, and only 8-plus-8 samplings in/out of the bend plane. Using this geometry, the pattern recognition code was run on two “toy” events containing 100 isotropic muons with momenta of 1 GeV/c and 2 GeV/c, respectively, and also on a more realistic 2-jet event, at 500 GeV centre-of-mass energy, which was generated by the PYTHIA event generator.

The isotropic events were intended to test the performance of the algorithm on high multiplicity events with soft tracks, for which the large bend angles and large MCS deviations make the pattern recognition more difficult than for stiff tracks. The 2-jet event gives a somewhat complementary test, with tightly collimated tracks of higher momentum.

For more detail on these test events, the tracks were propagated through the tracker using the GEANT detector simulation software package. Realistically simulated [7] noise tracks from incoherent beam electron pairs were overlaid on the event. The simulation included realistic Coulomb scattering (Moliere theory), Gaussian resolution smearing of 5 microns r.m.s. and 2 percent detector inefficiency per pixel or microstrip layer. Delta rays were generated down to a 1 MeV threshold, but other interactions and decays were not considered. In addition, ghost hits due to ambiguities in the stereo strips were not included.

Even for this non-optimal algorithm, the study found an acceptable track-finding efficiency of 99.6 percent: one track lost from the fiducial volume out of 225 tracks with momenta of 1 GeV/c or greater. (The lost track was from the event with 100 isotropic 2 GeV/c muons.)

Further pattern recognition studies, using higher track statistics and a more complete physics model, are needed before definitive conclusions can be drawn. However, it is reasonable to assume that the change to 10 detector layers along with improvements in the pattern recognition algorithm should provide extremely efficient and robust pattern recognition.

5 Mechanical Issues

Most of this section addresses the mechanical support structure of the CT, giving an overview of the support structure and then describing a finite analysis computer study of the rigidity of the structure. The section ends with a rough calculation of the space needed to route electronic and cooling services out the ends of the tracker.

Today's vertex detectors are stable at the level of a few microns during data-taking runs. A similar level of stability must be achieved over the much larger dimensions of the CT if the momentum resolution of the tracker is not to be degraded. Finite element stress calculations indicate that such a level can be achieved using 3-dimensional support structures of carbon fibre composite (CFC), as discussed below.

The crucial property of CFC is its extremely small temperature expansion coefficient: as low as $2 \cdot 10^{-7}$ per degree centigrade – which is roughly two orders of magnitude lower than metals. This allows the construction of metre-scale CFC structures which have an intrinsic thermal stability the same as, or better than, that of the few-centrimetre-scale beryllium support structures currently used in many vertex detectors.

With a Young's modulus of up to $200\,000 \text{ N/mm}^2$ (the same as steel)

and a radiation length of about 24 cm, CFC also has the stiffness required for building a light structure that won't add more than about one percent of a radiation length to the tracker mass. In addition, it is radiation hard and is easy to handle and machine.

With the thermal behaviour already taken care of, any other mechanical stress in the structure can be minimized by mechanically isolating the tracker. To achieve this, the CT will be supported at both ends on the tungsten mask, with one end fixed to the mask but the other end mounted on rollers to allow free movement parallel to the beamline. Any movement of the tungsten masks will move the CT as a whole, without distorting its shape or degrading its resolution. (It should be noted, however, that transverse motion of the masks can still degrade the knowledge of the beam-spot position.) We will return to describe a study of the CT's mechanical rigidity, after first giving details about the structural layout.

The large-scale structure of the CT consists of six modules. Firstly, the tracker splits in two, in a vertical plane through its long axis, to allow assembly and dis-assembly around the beam-pipe and tungsten radiation masks. Then, each of the halves is radially divided into three concentric sections: the innermost section consists of the 6-layer vertex detector and the other 2 sections each support 2 of the 4 large shells of detectors – shells 7 and 8 (9 and 10) for the smaller (larger) of the modules, counting outwards from the IP.

The ends of the six CT sections can be very rigidly joined to conical support structures lying directly over the tungsten mask. This is outside the active volume of the tracker, so thick CFC struts can be used without degrading the tracker performance.

The mechanical design of the vertex detector can be patterned after that of the (similar) BaBar silicon vertex tracker [5]. The BaBar tracker will use six mechanical modules, forming sextants in the azimuthal direction, which each contain several silicon detectors glued to CFC support beams. Some of the support beams will run within detector layers and others run radially between layers, and the modules will be attached to CFC support cones at the ends of the vertex detector.

The two large modules in each half of the CT consist of 3-dimensional structures of CFC struts, with triangular tetrahedra used as the basic structural unit. This ensures that the structure cannot flex in any direction without either compressing or stretching some of the struts. Both types of modules are tiled with the silicon detectors on both their inner and outer surfaces. In more detail, longitudinal CFC ribs, which are glued to the space structure, will support the semi-circular arcs of detectors, each of which will consist of several CFC modules containing a convenient number of detectors.

A mechanical design study has been made for an example layout of the larger of the two types of 3-D modules [10], since this is assumed to be the most demanding part of the CT mechanics. (To be precise, the layout was for an earlier iteration of the CT, which had the slightly smaller radius of 85 cm. However, the results from the study should also be approximately correct for the current design.) The example module comprised approximately 120 CFC struts along the ellipsoidal surface of shell 9, 160 struts along shell 10 and approximately 160 further struts joining the shells. The cross-sections of these 3 classes of struts were 1, 4 and 1 square centimetres, respectively, which corresponds to an average of less than 1 percent of a radiation length per shell.

It is difficult to specify and quantify the exact stresses on the tracker during data-taking. Since the CT is mechanically isolated, however, it is reasonable to assume that the time-dependent stresses should be much less than the constant gravitational stress from the weight of the tracker. Hence, the sag of the structure under its own weight acts as a very conservative benchmark for how much it could distort during data taking.

Finite analysis calculations for the example module, using the CASTEM2000 [12] software package, determined the maximum gravitational sag of the structure to be approximately 5 microns for an assumed weight of 400 kg. (The assumed weight is probably too large by at least a factor of two.) Figures 3 and 4 show two views of the example module, including a greatly magnified illustration of the nature of the gravitational sag.

The results of the finite element calculations suggest strongly that the tracker performance will not be adversely affected by distortions in its large-scale mechanical structure. If anything, an even lighter version of the 3-D mechanical structure would probably give sufficient rigidity.

As a final mechanical design issue, sufficient space must be provided for the routing of cables and cooling pipes out of the CT ends. The following crude calculation suggests that this will probably not be a serious problem.

The 2×10^7 channels of microstrip detectors will typically draw about 2 mW per channel [1], or 40 kW in total. If APS's are used in the vertex detector then they might be expected to consume of order 0.5 W.cm^{-2} [1, 2], adding about 10 kW to the total power consumption. (CCD pixels would require much less power [8].) From the Ohmic heating law ($P = IV$, in obvious notation), this power consumption corresponds to a current of 5000 A for an assumed average voltage drop of order 10 V. From Ohm's law,

$V = IR$, a total cross-section of only 10 cm^2 of aluminium conductor (resistivity of $2.7 \times 10^{-8} \Omega \cdot \text{m}$ at 300 K) would suffice to supply this current, with a manageable voltage drop of about 1 volt every 7 m.

The 10 kW power consumed by the front-end electronics will appear as heat. In a realistic scenario, this could be removed by a 60 cm^2 cross-section of water (which has a specific heat of $4.2 \text{ J} \cdot \text{K}^{-1} \cdot \text{cm}^{-3}$) flowing at 1 meter per second and with an average temperature rise of approximately 2 degrees centigrade.

To obtain the total space requirements for these services, the aluminium and water cross-sections must be multiplied by factors to account for cladding, load safety factors, additional services and packing efficiency. A crudely estimated total space requirement of around 500 cm^2 would result from safe multiplicative factors of 20 to 30 for the aluminium cross-section and 4 to 5 for the cooling water. This area corresponds to a 2 cm-thick annular aperture, with 20 cm radius, at each end of the tracker. Thus it appears that the routing of services from the tracker will make only fairly modest demands on the tracker geometry.

6 Alignment

Knowledge of the wafer positions at the level of one or two microns is required to keep pace with the excellent point precisions of the silicon detectors. This demanding specification seems to be achievable, given that the solid state technology and the stiff mechanical structure ensure that the alignment constants won't change with time.

Precise mounting of the wafers, followed by an optical survey, fixes the

radial alignment constants but cannot give the required accuracy in the transverse directions. The additional information must come from high statistics fitting of charged tracks, which, in turn, implies the need for dedicated calibration running on the Z^0 resonance, at 91.2 GeV centre-of-mass energy. (It should be noted that a strong physics case can also be made for a high statistics Z^0 run.) We now give a general overview of how the alignment could proceed.

The alignment procedure can be conceptually divided into two parts, with one part concentrating on local coordinate distortions and the other part concerning the more global alignment. The local alignment of neighbouring wafers within shells is attained by iteratively adjusting the transverse alignment constants to minimize the sum of the track chi-squares. This should be greatly aided, in this particular tracker, by the precisely known, time-independent geometry of the silicon wafers and by their overlap in both views.

Although effective for removing local misalignments, it is well known that a chi-squared minimization cannot completely determine the wafer positions, even in principle. The particular remaining global distortions which can degrade the momentum resolution of the tracker are rotations of the mid-radius shells relative to the inner and outer shells. In this case, the momenta of one sign of tracks will be under-measured and the opposite sign over-measured, but without necessarily increasing the tracks' chi-squared.

The second part of the track-based alignment procedure, which removes these distortions, uses the sample of back-to-back pairs of 45.6 GeV/c muons from decays, at rest, of the Z^0 . Consider two such muons from different Z^0 events, with opposite signs and which happen to have the same coordinates

in the innermost and outermost shells. It is clear that these muons will then have coordinates in the intermediate shells which are symmetrically displaced on either side of a straight line. Thus, a simple average of the hit positions gives an un-biased alignment for the intermediate shells. This general procedure assumes only that the Z^0 's are produced, on average, at rest and is true even in the presence of initial- and final-state radiation and a forward-backward muon asymmetry.

The order-of-magnitude integrated luminosity required for each alignment run can be calculated under the reasonable assumption that the final alignment step requires the most luminosity, since it can only use the dimuon channel. The total number of muon pairs required for the alignment can be estimated as the product of two terms, one for the alignment in a given direction and the other to take account of the effective number of different directions in which the final alignment step must be done, as follows.

Under the idealized assumption of monochromatic muon tracks of very high energy, only one track of each sign would be required to determine the alignment in any given direction to an accuracy equal to the point resolution. (To be precise, the alignment uncertainty would actually be a factor of $1/\sqrt{2}$ better than the point resolution.) More realistically, multiple scattering is still important for the 45.6 GeV muon tracks from Z^0 decays at rest, and additional statistics might also be needed due to a non-zero spread in the transverse momenta distributions. Since we also wish the alignment to be determined much more accurately than the point resolution, we conservatively assume that 100 muons of each sign would determine the alignment well enough in any specified direction.

It is to be expected that independent misalignments would generally exist

at widely spaced polar angles, but, on the other hand, but it is likely that any azimuthal variation would already have been corrected for by requiring the momentum spectra of all charged tracks to be azimuthally symmetric. A fairly conservative assumption is that each of the bands of wafers in the outer shell (37 bands, for 10 cm long wafers) would effectively need a separate alignment constant. This corresponds to of order 100 “independent directions”.

Multiplying the factors predicts that of order 10 000 muon pairs would suffice to do the final alignment step to much better than the point precision of the tracker. Since the cross-section-times-branching-ratio for dimuons at the Z^0 resonance is about one nanobarn, this corresponds to an integrated luminosity of order 10 inverse picobarns, or 10^4 to 10^5 seconds of running at realistic FLC luminosities of 10^{33} or 10^{32} $\text{cm}^{-2}\text{s}^{-1}$.

In summary, it appears that the CT could be accurately aligned with only a short run at the Z^0 peak, say, once every year.

7 Central Tracker Performance

This section uses heuristic arguments to derive simple expressions for the vertexing and momentum resolutions of the CT as a function of polar angle. A slightly more rigorous estimate of the momentum resolution for high momentum tracks is also presented.

Considering first the vertexing performance, a simple parameter which gives a good indication of the performance of the vertex detector is the width, σ_{ip} , of the measured impact parameter distribution for tracks originating from the IP. (More precisely, σ_{ip} is the width in either the r-phi or z projection.)

The impact parameter uncertainty will have contributions from both the point resolutions of the pixel detectors and from multiple coulomb scattering (MCS) in the beam-pipe and detector material, so a standard general form is:

$$\sigma_{ip} = a(\theta) \oplus b(\theta)/p, \quad (1)$$

where p is the track momentum, θ the polar angle of the track, and the terms in a (point resolution term) and b (MCS term) are added in quadrature. The parameters may be estimated by considering the asymptotic limits of extremely high momentum and low momentum tracks, where the first or second terms will dominate, respectively.

MCS can be neglected in the high momentum limit, so the direction of tracks can be very precisely measured using the full lever-arm of the outer tracker. Out of the bend plane, the outermost position determinations will have uncertainties of order 100 microns (depending on the stereo angle chosen for the microstrips) at a lever-arm of about 1 metre, corresponding to an angular uncertainty of only 0.1 milliradians. In the bend plane, resolutions of a few microns for both the mid- and outer-radius shells should give an even better angular measurement, even allowing for the curvature of the track in the magnetic field. For determining the impact parameter, these angular uncertainties will be multiplied by the extrapolation distance from the vertex detector to the IP – a few centimetres – which will give a contribution of a few microns to σ_{ip} .

A comparable contribution to σ_{ip} in the high momentum limit will come from the point resolution of the 6 planes of vertex detector (i.e. $1/\sqrt{6}$ times the point resolution of an individual plane). Hence, on adding the two contributions in quadrature, one might expect the high-momentum limit of the

impact parameter resolution to be of order:

$$a(\theta) \simeq 5 \text{ microns}, \quad (2)$$

with little dependence on polar angle.

To estimate the MCS term in σ_{ip} , consider that very low momentum tracks will scatter through a relatively large angle at the innermost layer of the tracker. The average angle is given by [11]:

$$\theta_{MCS} \simeq 0.0136\sqrt{X_0/p}(\text{GeV}/c), \quad (3)$$

where X_0 is the fraction of a radiation length of material contained in the beampipe plus innermost layer of pixels. The average extrapolation error to the IP is the product of θ_{MCS} and the distance to the first layer. At normal incidence, $\theta = 90^\circ$, this distance is the radius of the first layer:

$$b = \theta_{MCS} \times (\text{radius of layer 1}). \quad (4)$$

Assuming a radius of 2 cm and a reasonably conservative thickness of 1 percent of a radiation length [2, 8] (this is for APS's – CCD's can be made considerably thinner) gives:

$$b(90^\circ) \simeq 30 \mu\text{m}.\text{GeV}/c. \quad (5)$$

For smaller angles of incidence, $b(\theta)$ will become larger due to the increased extrapolation distance to the IP and to traversing a greater thickness of material. In the central region, where the innermost layer is a barrel, it is easily seen that the angular dependence goes as [8]:

$$b(\theta) \simeq 30/(\sin \theta)^{3/2} \mu\text{m}.\text{GeV}/c. \quad (6)$$

In moving to smaller polar angles, the resolution will undergo discontinuities at the ends of shells 1 and 2 which are not reproduced by this simple form. The equation is, however, a reasonable starting point for simple studies of the physics potential of the vertex detector.

For physics analyses using today’s vertex detectors, the tails on the impact parameter distributions are often at least as important as the widths of the distributions. Hopefully, the resolution tails should be very much reduced for the CT vertex detector, with 6 layers of pixels rather than 2 or 3 layers of microstrips. (The SLD vertex detector has already demonstrated the advantages of pixels for obtaining smaller, better-modelled resolution tails [8].)

On comparing the numerical values of the constants a and b , it can be seen that the MCS and point-resolution contributions to σ_{ip} are of similar size for track momenta of several GeV/c. Since some of the tracks with lifetime information will be in this momentum range, it is clear that both terms will be relevant for physics analyses. It also appears that the impact parameter resolution is good enough to give a very high efficiency and purity for finding beauty and charm vertices and even for flagging the tracks from 1-prong decays of tau leptons (86% of all tau decays). This can be shown using a heuristic argument, as follows.

From relativistic kinematics, a relativistic particle with lifetime-at-rest τ will survive for an average distance $L \simeq \gamma c\tau$, with c the speed of light and γ the relativistic boost. Also, the forward hemisphere of the particle’s rest frame is compressed, in the lab frame, into a cone of half-angle $1/\gamma$. Thus, the “typical track” in a “typical decay” will have an impact parameter of $L/\gamma = c\tau$, independent of the relativistic boost. The “typical” impact

parameters for B hadrons ($c\tau \simeq 450 \mu\text{m}$), charm hadrons ($c\tau = 320 \mu\text{m}$ for D^+ , $130 \mu\text{m}$ for D^0), and tau leptons ($c\tau = 91 \mu\text{m}$), are all seen to be much larger than the several micron uncertainty in the resolution. This suggests that identifying the “typical” decay topologies will not be too difficult, even for tau decays. Instead, the challenge will be to push for very high efficiency and purity by identifying those decays with shorter-than-average lifetimes and small impact parameters.

We now move on to a discussion of the performance of the CT for measuring track momenta, again using simple heuristic arguments to derive numerical expressions for the momentum resolution. The general form of the momentum resolution equation is expected to be [11]:

$$\sigma(p_t)/p_t = c(\theta) \oplus d(\theta) \times p_t, \quad (7)$$

where p_t is the component of the momentum transverse to the B field, and the constants c and d represent the contributions from MCS and point resolutions, respectively.

The easiest way to derive approximate values for the two constants is to use the simplified model of three track position measurements: one at each of the inner-, mid- and outer-radii. (To be precise, the radius is defined in the plane transverse to the magnetic field, so it is a function of the polar angle.) If the three measurements are labelled f , g and h , respectively, then the measured quantity which is related to the track momentum is the sagitta, S , defined by:

$$S = (f + h)/2 - g. \quad (8)$$

Starting from the Lorentz force equation, it is easy to derive the following expression for the sagitta in terms of the magnitudes of the magnetic field

strength (B), transverse momentum (p_t), charge (q) and half-radius in the transverse plane ($L(\theta)$):

$$S = L(\theta)^2 q B / 2 p_t. \quad (9)$$

(A small angle approximation has been used, and the form of the magnetic force equation is that appropriate for MKS units: $F = qvB$.) For a singly charged track, with S and L in metres, B in Tesla, and converting momentum units to GeV/c, this becomes:

$$S = 0.150 L(\theta)^2 B / p_t (\text{GeV}/c). \quad (10)$$

It follows that the value of d can be evaluated from

$$d(\theta) = \sigma_{S,point} / (0.150 L(\theta)^2 B), \quad (11)$$

with the uncertainty in the sagitta for high momentum tracks, $\sigma_{S,point}$, given by the sum-in-quadrature of the uncertainties in the terms of equation 8:

$$\sigma_S = \sigma_f / 2 \oplus \sigma_h / 2 \oplus \sigma_g. \quad (12)$$

The CT at normal incidence to the beamline has $L \simeq 0.5$ metres, $B = 4$ Tesla and $\sigma_{S,point} \simeq 8$ microns, so

$$d(\theta = 90^\circ) \simeq 5 \times 10^{-5} (\text{GeV}/c)^{-1} \quad (\text{estimated}). \quad (13)$$

As confirmation of this equation, a more precise value,

$$d(\theta = 90^\circ) \simeq 3.6 \times 10^{-5} (\text{GeV}/c)^{-1} \quad (\text{fitted}), \quad (14)$$

was obtained [13] for $d(\theta = 90^\circ)$, using the MINUIT fitting software [14] with the assumption of one hit per detector layer and effective point resolutions

(i.e. including misalignments) of 8 microns per detector. (No beam constraint was used.)

For the angular dependence of d , one can take advantage of the simple dependence of the tracker geometry on polar angle: the radial distance to each of the detector shells scales in approximate proportion to the radial distance to the outermost shell, $R(\theta)$, and the outermost shell is an ellipsoid:

$$(Z(\theta)/A)^2 + (R(\theta)/B)^2 = 1, \quad (15)$$

with $A = 1.74$ m and $B = 1.00$ m. All of the above equations still apply, with

$$L(\theta) = R(\theta)/2, \quad (16)$$

so,

$$d(\theta) = d(90^\circ) \left\{ \frac{R(90^\circ)}{R(\theta)} \right\}^2. \quad (17)$$

Using the explicit angular dependence of R for the ellipsoid,

$$1/(R(\theta))^2 = \cot^2 \theta / A^2 + 1/B^2, \quad (18)$$

and putting in the numbers for the CT gives the explicit angular dependence:

$$d(\theta) = 3.6 \times 10^{-5} \{0.33 \cot^2 \theta + 1\} (GeV/c)^{-1}. \quad (19)$$

This estimate is found to agree well with the fitted values for several polar angles.

The MCS term, $c(\theta)$, depends on the distribution of mass in the tracker, so it is slightly more difficult to estimate. Material near mid-radius clearly contributes much more to the momentum uncertainty than material near the inner and outer radii. In the simplified model, the uncertainty in the outer endpoint due to a scattering centre between mid-radius and outer-radius is

clearly just the average scattering angle times the lever-arm distance to the outer radius:

$$\delta h = (\text{lever arm}) \times \theta_{MCS}. \quad (20)$$

(A corresponding equation holds for scattering centres inside mid-radius.) For the worst case, a scattering centre of X_0 radiation lengths at mid-radius (lever-arm distance = L) one gets, on combining equations 3, 7 and 20:

$$c(\theta = 90^\circ) = 0.045\sqrt{X_0}/(L(\theta).B). \quad (21)$$

On putting in the numbers for the CT and using the reasonable guess that the amount of scattering material around mid-radius corresponds to 4 percent of a radiation length at mid-radius, one finds:

$$c(\theta = 90^\circ) = 0.0045. \quad (22)$$

The simple geometry of the CT again allows an explicit parameterization of $a(\theta)$. If $D(\theta)$ is the distance from the IP to the edge of the tracker for polar angle θ then

$$\begin{aligned} c(\theta) &\propto D(\theta).D(\theta).\frac{R(\theta)}{D(\theta)}.\frac{1}{R(\theta)^2} \\ &\propto D(\theta)/R(\theta) \\ &= 1/\sin(\theta). \end{aligned}$$

The interpretation of the terms is as follows. The first factor of $D(\theta)$ comes from the increasing material at smaller polar angle, using equation 3 and the convenient and rather conservative assumption that the average density of material is proportional to $D(\theta)$. The second factor of $D(\theta)$ is the lever-arm for scattering (equation 20). The third term, $R(\theta)/D(\theta)$, accounts for the fact that the scattering angle depends on the track's total momentum, rather

than just the transverse component. The final term, $1/R(\theta)^2$, is simply the decrease in the sagitta given by equations 9 and 16. Hence,

$$c(\theta) \simeq 0.0045/\sin(\theta). \quad (23)$$

To summarize this section, the impact parameter resolution and momentum resolution are valuable indicators of the performance of the CT. Using heuristic arguments, explicit values for these parameters were estimated as a function of polar angle:

$$\sigma_{ip} \simeq 5 \oplus 30/(\sin \theta)^{3/2}/p(\text{GeV}/c) \quad \text{microns}, \quad (24)$$

and,

$$\sigma(p_t)/p_t \simeq 0.0045/\sin(\theta) \oplus 3.6 \times 10^{-5}\{0.33 \cot^2 \theta + 1\} \times p_t(\text{GeV}/c). \quad (25)$$

8 Central Tracker Cost

The cost of the CT should be completely dominated by the cost of the silicon detectors and associated electronics, with the mechanical structure of the CT probably contributing less than 1 MDM (million Deutchmarks).

For illustration, carbon fibre struts suitable for the 3-D support structures cost about 250 Swiss Francs per metre, with little dependence on cross-section [22]. At this price, the large 3-D structures supporting the two outermost shells contain a total of only about 30 000 DM worth of carbon fibre composite.

Large uncertainties in the cost of solid state detectors and associated electronics preclude a detailed cost estimate for the CT. Fortunately, prices for

these components are rapidly dropping as the technology advances, so an estimate based on today's prices is almost certain to be inflated. A conservative over-estimate is obtained from the cost calculations used for the CMS [15] and ATLAS [16] experiments. In particular, the radiation environment at the LHC requires very high quality silicon wafers and very specialized electronics, which will not be needed at the TLC.

Crudely scaling the total cost of the ATLAS silicon central tracking, 31 MCHF (million Swiss Francs), by the ratio of the detector areas – 96 m² for the CT and 42 m² for ATLAS – gives a microstrip cost of 71 MCHF. This cost includes the detectors, 20 percent spare detectors, electronics for the read-out, mechanical support and installation. Similarly, scaling the cost of the ATLAS APS's, 13 MCHF, by the ratio of areas (1.75 m² for the CT and 4.1 m² for ATLAS) adds an additional 6 MCHF to the total cost. (Using CCD's instead of APS's would somewhat reduce the vertex detector cost.)

Summing the contributions from the mechanical support structure, silicon microstrips and pixels gives a total tracker cost of a little less than 80 MCHF. As already discussed, this can be considered to be a conservative upper bound and the true cost is likely to be less than this.

9 Detector Design for 500 GeV e⁺e⁻ Collider

This rather long section presents an example of a detector design which incorporates the CT described above and which would be suitable for the proposed DESY electron-positron collider or a similar accelerator. Besides its intrinsic interest, this exercise demonstrates that the CT design is compatible with an affordable, high performance detector and also motivates some of the param-

eters used in the CT studies – such as the 4 Tesla magnetic field. However, it should be emphasized that the detector design has not been studied at the same level of detail as the central tracker. It is quite conceivable that better options exist for some of the other subdetectors.

Figure 5 is an illustration of the detector. The design is similar in some ways to the CMS detector, which also uses a crystal electromagnetic calorimeter (ECAL) and a 4 Tesla magnet. However, the central region of CMS is less projective and CMS has the hadron barrel calorimeter (HCAL) inside the magnet.

Subsections 9.1 through 9.4 describe the subdetectors outside the central tracker: the electromagnetic calorimeter, magnet, scintillating tile arrays and hadron calorimeter. Subsection 9.5 gives an overview of the detector performance, subsection 9.6 addresses the mechanical structure of the detector and subsection 9.7 gives a rough estimate of the detector cost, before the section is summarized in subsection 9.8.

9.1 Electromagnetic Calorimeter

The electromagnetic calorimeter (ECAL) consists of an ellipsoidal array of lead tungstate scintillating crystals, read out by avalanche photodiodes. This choice is motivated by the excellent energy resolution for electromagnetic showers:

$$\sigma(E)/E = 0.5\% \oplus 2\%/\sqrt{E(\text{GeV})} \quad (26)$$

and compactness (a radiation length of 0.89 cm and Moliere radius of 2.2 cm) of these crystals.

Additional attractive properties of lead tungstate are: fast scintillation emission, good radiation hardness and a substantial existing production ca-

pability. It should be noted, however, that achieving a stable, uniform calibration for the crystal array is known to be a difficult challenge. In this respect, the ECAL may benefit from experience gained at the ZEUS detector, which is considering installing a small array of these crystals as a forward electromagnetic calorimeter. The CMS detector also intends to use lead tungstate crystals for its ECAL, and is already undertaking a great deal of research into the performance of these crystals.

Reasonable dimensions for the crystals [17] are a depth of 28 radiation lengths (25 cm) and transverse dimensions equal to the Moliere radius ($22 \times 22 \text{ mm}^2$). The crystals are oriented to be projective to the IP, and cover an ellipsoidal surface just outside the central tracker, with an inner surface which can be parameterized as:

$$(x^2 + y^2)/1.10^2 + z^2/1.94^2 = 1 \quad (27)$$

(with position coordinates x, y and z in units of metres and the z axis along the beam-line).

The position resolution for electromagnetic showeres is predicted to be approximately $2.2 \text{ mm}/\sqrt{E}$ [17]. Using equation 27, it can be seen that this corresponds to an angular resolution of $2.0 \text{ mr} \cdot (\text{GeV})^{1/2}$ in a direction perpendicular to the beamline, improving smoothly to $1.2 \text{ mr} \cdot (\text{GeV})^{1/2}$ at the calorimeter edge – 120 mr from the beam direction.

The mechanical support of the crystals could proceed along the lines of that used for the L3 crystal calorimeter and the structure proposed for the CMS ECAL [1], with the crystals sandwiched between inner and outer support frames. In the central region of this ECAL, each crystal is held in place by an axial force applied to its back face using a spring-loaded pusher. Each pusher encloses an avalanche photodiode, thermometer and optical fibre

for monitoring the crystal calibration. A hemi-spherical plastic end-cap on the front face of each crystal, which presses against the contoured surface of the inner support frame, distributes the pressure evenly over the crystal face. The crystals in the forward region could be stacked as in conventional end-cap calorimeters.

Following CMS, the inner support frame could consist of carbon-fibre composite and hexel honey-comb, and the outer support frame of aluminium. For this detector, the support frames would be half-ellipsoids, with the ECAL split in two halves along a plane perpendicular to the beam-line and passing through the IP. The smaller ends of ellipsoids would be attached to the tungsten mask and the larger ends of the outer ellipsoids would be supported on rails attached to the inner surface of the magnet. As in CMS, the crystals themselves would contribute to the rigidity of the structure, preventing the light inner support frame from flattening under the weight of the ECAL.

As a specific example of a procedure for assembling the calorimeter, each of the two inner support frames could be constructed as a single piece but the outer frames must be segmented to allow assembly and dis-assembly of the crystal array and access to the electronics. The crystals could be positioned and aligned beginning at the small ends of the ellipsoids and proceeding row-by-row towards the middle of the ECAL.

9.2 Magnet and Scintillating Tile Arrays

Situated just outside the crystal calorimeter, the 4 Tesla superconducting solenoidal magnet has an inner radius of 1.55 m, half-length of 3.25 m and is 2.5 radiation lengths thick (using the approximate formula given in [18]). The strong magnetic field improves the momentum resolution of the tracker

and also reduces the background in the vertex detector by confining most of the soft beamstrahlung tracks to remain inside the beam-pipe.

The length of the magnet was determined from the magnet radius and CT length according to the formula:

$$L_{\text{magnet}} = L_{\text{tracker}} + 2 \times R_{\text{magnet}}. \quad (28)$$

The motivation is that the magnetic field inside a solenoid is relatively uniform up to about R_{magnet} from the ends. (This formula is approximately obeyed by the CMS magnet, which will also be 4 Tesla.) This argument might be somewhat conservative, and the magnet can be shortened if calculations show that this won't adversely affect the field in the forward region of the central tracker.

Because the magnetic field inside the solenoid is much stronger than the saturation field for iron (1.5 to 1.8 Tesla) it should be little affected by the iron flux return outside the magnet. Thus, one can approximately calculate the fields along the z axis by assuming a solenoidal field in a vacuum. A simple analytic calculation predicts that at the maximum z of the inner tracker, 1.70 m, the field along the beam axis has fallen by only 8%, giving good field uniformity for tracking. Further out, fields are 3.5 T at 2m (the position of the innermost quadrupole magnet for the S-band accelerator option) and 2.5 T at 3m (the position of TESLA's innermost quadrupole). This seems to be safely below the 3 Tesla limit imposed for the TESLA option. In the S-band option, the innermost accelerator magnet is assumed to be shielded by a compensating solenoid, so the situation is less clear.

Scintillating tile arrays, placed immediately inside and outside the magnet, provide longitudinal and transverse sampling of hadronic showers and should minimize the effect of the 0.6 interaction lengths of dead material.

The tile dimensions could be as small as 10 cm by 10 cm, which would correspond to about 5000 tiles in each of the two layers. A typical configuration would consist of a wavelength-shifting fibre embedded in the tile surface and connected to several metres of clear fibre. Once outside the detector, the clear fibres could be read out, for example, by either conventional multi-anode phototubes or by Visible Light Photon Counters (VLPC's) similar to those being installed for the scintillating fibre tracker of the D0 experiment. VLPC's are a variant of the solid state photomultiplier tube which operates in a liquid helium cryostat. They provide greater than 70% quantum efficiency for visible light, with a gain of roughly 20 000 and a rate capability of at least 10 MHz [19].

Assessing a cost of 300 DM per channel for the tiles and readout gives a total estimated cost for the two tile arrays of around 3 MDM.

9.3 Hadronic Calorimeter

The hadron calorimeter (HCAL) consists of a barrel region outside the magnet and two end-cap calorimeters with slanted, partially projective front faces to fit between the ellipsoidal ECAL and the magnet barrel. The end-caps reach in to about 48 degrees from the beam direction. Iron/scintillator sampling calorimetry is a likely choice for the barrel HCAL (as in ATLAS), with copper/scintillator calorimetry in the end-caps (like the CMS HCAL, which is also inside a 4 Tesla field).

Metal/scintillator sampling calorimeters are compact, well understood and offer very good energy resolution. Because of their relatively high densities, iron and copper are good choices for the metal absorber. Further study is needed to optimize the calorimeter depth and segmentation, and also to

decide whether a worthwhile improvement in performance would result from changing to an even denser absorber, such as depleted uranium.

Hadronic energy resolutions of $45\%/\sqrt{E}$ (ATLAS) [2] and $65\%/\sqrt{E}$ (CMS) [1] have been estimated for the calorimeters themselves. Further study is needed to estimate the performance when placed behind both lead tungstate crystals and 0.6 interaction lengths of magnet sandwiched between scintillating tile arrays. (The lead tungstate crystals are a little more than one interaction length, fully active but with an e/pi ratio of about 1.6.)

Some evidence that the dead material in the magnet should not seriously compromise the calorimeter performance is provided by the large coarse-sampling calorimeters used in accelerator-based neutrino experiments. The CCFR calorimeter uses liquid scintillation sampling every 10 cm of iron – that is, every 0.6 interaction lengths and 6 radiation lengths – so each sampling length in the CCFR calorimeter includes more material than in the entire thickness of the TLD magnet. In spite of the coarse sampling, the CCFR energy resolution measured in hadron test beams [20] is a moderate $85\%/\sqrt{E(\text{GeV})}$, with only very small resolution tails for shower energies of order 100 GeV or above.

9.4 Flux Return and Muon Chambers

The material in the flux return – approximately 2 m of iron – serves as a hadronic filter for muon identification. The inner part can also be instrumented as a hadronic tail-catcher if studies suggest this is necessary.

In general, substantially lower demands are placed on the muon identification systems at electron-positron colliders than at hadron colliders, due to the much reduced backgrounds from punch-through hadrons. The muons

could be tracked using hermetic layers of drift tubes at the outer radius and also, perhaps, at the mid-radius of the flux return. The CMS chambers seem to provide a reasonable starting design: 8 (4) layers of drift tubes parallel (perpendicular) to the beam direction plus resistive plate chambers for triggering and timing.

The iron surrounding the HCAL provides a return path for the field lines from the solenoidal magnet and also ranges out hadrons that have penetrated the HCAL and would otherwise constitute a background for muon identification. The minimum thickness of the flux return is 12 interaction lengths, at $z=0$, which ensures that the entire detector presents at least 20 interaction lengths to hadrons originating from the collision region. In the forward region, 2 m of iron is about what is necessary to contain the field emanating from the solenoid. The iron cross-section at the radius of the magnet is about 2.5 times the inner cross-section of the magnet, corresponding to an average magnetic field, about 1.6 T, which is close to saturating the iron.

A detailed knowledge of the magnetic field in the iron would require a finite element calculation on a computer. However, it is expected that the detailed geometry of the flux return should not seriously affect the magnetic field distribution in the central tracker volume, since the magnet extends well beyond the tracker and the 4 T magnetic field is well above saturation for iron. Hence, the design of the flux return can be rather freely optimized for muon detection.

9.5 Detector Performance Overview

Operating at the energy frontier for electron-positron collisions demands a detector with very good all-around performance, since it is not known which

new physics processes might present themselves. Table 1 summarizes the approximate estimated values, taken from preceding sections, of some of the most important resolution parameters associated with each subdetector or event reconstruction task. The corresponding values are also given for the ALEPH detector [21] at the LEP accelerator, allowing a direct comparison between the TLD and a detector operating at the current electron-positron energy frontier. In spite of the very approximate nature of the comparison, it can be seen that the proposed detector performs significantly better in most areas and is not worse for any of the parameters. This improvement can mostly be attributed to recent progress in detector technologies.

9.6 Mechanical Structure and Detector Assembly

The mechanical design of the detector support structure is intimately related to the procedure chosen for assembling and dis-assembling the detector. Detailed planning of the assembly procedure would involve a more complete knowledge of the detector-machine interface than is now available. For the moment, only a general outline will be given for a procedure which seems to provide a good starting point for more detailed planning.

The outer part of the detector – the barrel region of the HCAL, the flux return iron and the muon chambers – splits vertically in two along the major axis of the detector. These “clam-shells” are self-supporting and rest on rails which allow them to be retracted in a horizontal direction perpendicular to the beam-line. A sector at the bottom of the outer detector would remain in place, supporting the magnet and inner detector. Special arrangements would have to be made to access the electronics channels in this sector – this should not be a major design problem.

parameter	σ_{TLD}	σ_{ALEPH}	$\sigma_{\text{TLD}}/\sigma_{\text{ALEPH}}$
CT Impact Parameter:			
high mom. tracks	5 μm	25 μm	0.20
low mom. tracks	30 $\mu\text{m}.\text{GeV}/c$	95 $\mu\text{m}.\text{GeV}/c$	0.32
CT Momentum Resol.:			
high mom. tracks	$0.36 \times 10^{-4} (\text{GeV}/c)^{-1}$	$6 \times 10^{-4} (\text{GeV}/c)^{-1}$	0.06
low mom. tracks	0.0045	0.005	0.90
EM Energy Resol.:			
high energy limit	0.005	0.019	0.26
stat. term ($1/\sqrt{E}$)	0.02 $(\text{GeV})^{1/2}$	0.18 $(\text{GeV})^{1/2}$	0.11
EM Angular Resol.:			
stat. term ($1/\sqrt{E}$)	2.2 mr. $(\text{GeV})^{1/2}$	2.5 mr. $(\text{GeV})^{1/2}$	0.88
Hadronic Energy Resol.:			
stat. term ($1/\sqrt{E}$)	0.65 $(\text{GeV})^{1/2}$ (?)	0.85 $(\text{GeV})^{1/2}$	0.76 (?)

Table 1: **Approximate values for the uncertainties in some of the important resolution parameters of the TLD. For comparison, the corresponding uncertainties are also given for the ALEPH detector. The final column is the ratio of the uncertainties for the FLD and ALEPH. A value of 1.0 corresponds to equal performance, while a smaller value represents an improvement of the FLC over ALEPH.**

The inner detector is supported on the fixed rigid structure provided by the magnet, as in the CMS design concept. Rails on the inside surface of the magnet allow the inner detector to be withdrawn in two halves, with one half on each side of the IP. These rails can extend beyond the ends of the magnet, parallel to the beam axis and supported by the fixed bottom sector of the outer detector.

The order in which the inner-detector halves are withdrawn is important because the CT is only fixed to one side of the tungsten mask. The opposite side of the inner detector would be withdrawn first, with the CT resting in its original position. As the un-anchored side of the CT dropped off the receding mask it would be supported by cables connected to the fixed half of the ECAL, whose purpose is specifically to perform this task. Once the first detector half has been withdrawn sufficiently, the CT can be disassembled from the beam-pipe and removed for maintainance.

Each of the two inner-detector halves would consist of half of the ECAL, one side of the tungsten radiation mask, one of the HCAL end-caps and, optionally, end-cap sections of the iron flux return and muon chambers. These would be withdrawn as one piece, but a further set of rails between the ECAL and HCAL would allow these sub-detectors to be separated so that the ECAL electronics could be accessed.

To summarize, the dis-assembly of the detector could proceed as follows:

1. Retract the clam-shells of the outer detector.
2. Disassemble the nearby beam-line.
3. Retract one half of the inner detector.
4. Dis-assemble and remove the central tracker.

5. Retract the second half of the inner detector.
6. Separate the ECAL halves from the HCAL end-caps.

The detector would be assembled by simply following the inverse procedure.

9.7 Detector Cost Estimate

A rough cost estimate for the TLD is given in table 2.

The CT cost was taken to be approximately 80% of the conservative upper limit (80 MCHF) given in section 8. The ECAL, HCAL and flux return costs were obtained from the CMS values scaled by the detector volume and the muon chamber cost was scaled by area with respect to CMS. The magnet cost was calculated from a formula provided by Francois Kircher [18] and the cost of the scintillating tile arrays was taken from section 9.2. Finally, 5 MDM was added for the luminosity monitor and 10 MDM for the mechanical structure.

The total estimated detector cost is approximately 230 MDM. This is only about half of the cost of the CMS and ATLAS detectors at the LHC, which reflects the reduced costs for a smaller, more compact design.

9.8 Summary of Example Detector Design

A detector design has been presented which attempts to optimise the choice of subdetector technologies and general layout for a detector incorporating a compact all-solid state central tracker. The design seems to achieve the standard of all-around performance required for exploring physics at the electron-positron energy frontier. The central tracking and electromagnetic calorimetry should perform significantly better than most competing technologies,

subdetector	cost
central tracker	75 MDM
ECAL	50 MDM
HCAL barrel	30 MDM
HCAL end-caps	4 MDM
luminosity monitor	5 MDM
magnet	10 MDM
scint. tile arrays	3 MDM
muon chambers	23 MDM
flux return	20 MDM
mechanical structure	10 MDM
TOTAL	230 MDM

Table 2: **A rough cost estimate for the TLD detector.**

while the hadron calorimetry and muon identification performances are, at minimum, competitive with rival technologies. The cost of the detector also seems to be reasonable. Such a detector provides a reasonable starting place for detailed detector optimization and fine-tuning studies.

10 Conclusions

This report presents an all-solid state central tracker (CT) which provides both excellent momentum resolution and excellent vertexing. The tracker would be suitable for the proposed DESY 500 Gev electron-positron linear collider or a similar accelerator.

As discussed in section 2, the solid state detectors are arranged in 10 con-

centric ellipsoidal shells around the interaction point. The 6 innermost shells consist of pixel detectors and the 4 larger shells use silicon strip detectors in either small angle stereo or “U-V-X” geometry.

A detailed discussion of the solid state detector elements and associated electronics was given in section 3. They were found to be both technologically feasible and suitable for the tracker environment, with the required specifications representing only a modest extrapolation from existing detectors.

The complete absence of gas-based tracking elements allows a very robust tracker with no time-dependent calibration constants and with a very fast read-out. The possibility of including even faster trigger read-out channels means that the position information from the CT can be made quickly available to the event trigger logic.

The nearly projective ellipsoidal shell geometry provides smoothly varying tracking coverage down to small polar angles, avoiding discontinuities such as barrel-to-endcap cross-over regions. This geometry is consistent with a pattern recognition algorithm that is both simple and efficient, and with a light but stiff mechanical structure. Detailed descriptions of studies for the pattern recognition and mechanical structure were presented in sections 4 and 5, respectively.

All the tasks of the central tracker – track-finding, vertexing and momentum measurement – are performed using all the tracking layers simultaneously, which is both economical and removes many sources of systematic uncertainty.

The increased cost of solid state detectors, relative to cheaper but less performant gas-based detectors, seems to be greatly compensated by the

smaller size of the solid state central tracker. This allows the CT to be surrounded by smaller, and hence cheaper, high performance calorimeters and other subdetectors. To illustrate this, section 9 discusses an example of a reasonably priced yet high performance collider detector which is based around the all-solid state CT.

In summary, the central tracker described in this report seems to be both affordable and technologically feasible, and would be expected to provide state-of-the-art tracking performance for the next decade's collider detectors.

Acknowledgements

Many people at the CERN and DESY laboratories have contributed ideas and expertise to this work. Of these, Jacques Genest deserves special mention for his invaluable expert assistance with mechanical simulations of the central tracker. The ECFA/DESY linear collider workshops have also been very important in refining and improving the design of the central tracker. The author would particularly like to thank the CERN and Hamburg OPAL groups for their help and support.

References

- [1] The Compact Muon Solenoid Technical Proposal.
CERN/LHCC 94-38 (1994).

- [2] ATLAS Technical Proposal.
CERN/LHCC/94-43 (1994).

- [3] A summary of existing front-end chips for silicon microstrip detectors can be found in Chapter 4 of “The CLEO III Detector: Design and Physics Goals”,
[http : //w4.lns.cornell.edu/public/CLEO/CLEO3/CLEO3.html](http://w4.lns.cornell.edu/public/CLEO/CLEO3/CLEO3.html)

- [4] CEBAF Large Acceptance Spectrometer.
[http : //www.ceba.f.gov/clas/CLAS.html](http://www.ceba.f.gov/clas/CLAS.html) .

- [5] Technical Design Report for the BaBar Detector.
[http : //www.slac.stanford.edu/BFROOT/doc/TDR](http://www.slac.stanford.edu/BFROOT/doc/TDR).

- [6] Electron-Positron Collisions at 500 GeV: The Physics Potential.
DESY 92-123 and DESY 93-123.

- [7] D. Schulte Ph.D. Thesis, DESY. In preparation.

- [8] Vertex Detectors: The State of the Art and Future Prospects.
C.J.S. Damerell. RAL-P-95-008 (1995).

- [9] C.J.S. Damerell presentation. ECFA/DESY Mini-workshop
on the Proposed DESY 500 GeV Electron-Collider.
CERN, 6–7 May, 1996.

- [10] B.J. King presentation. ECFA/DESY Workshop on
the Proposed DESY 500 GeV Electron-Collider.
UCL London, 4–6 July, 1996.

- [11] The Particle Data Group,
Review of Particle Physics.
Phys. Rev. D54 (1996).

- [12] CASTEM200 was originally developed by the French
“Commissariat a l’Energie Atomique” (CEA).

- [13] Momentum Resolution Studies for a TPC-Based Central Tracker.
B.J. King, this DESY Report.

- [14] The MINUIT software package.
CERN Computer Centre Program Library.

- [15] CMS Cost Review, Version 5. January 19, 1995.
- [16] ATLAS Cost Planning, Version 4.1. May 10, 1995.
- [17] R.L. Brown presentation. ECFA/DESY Workshop on
the Proposed DESY 500 GeV Electron-Collider.
UCL London, 4–6 July,1996.
- [18] Francois Kircher presentation. ECFA/DESY Workshop on
the Proposed DESY 500 GeV Electron-Collider.
UCL London, 4–6 July,1996.
- [19] DO Experiment, Upgrade Information.
[http : //d0sgi0.fnal.gov/hardware/upgrade/upgrade.html](http://d0sgi0.fnal.gov/hardware/upgrade/upgrade.html) .
- [20] W.K. Sakumoto *et al.* (CCFR collab.),
Nucl. Inst. Meth. A294 (1990) 179.
- [21] Performance of the ALEPH detector at LEP.
The ALEPH Collaboration.
CERN-PPE/94-170 (1994).

[22] Private communication with Hubert Gerwig, CERN.

All-Solid State Central Tracker: x-z View

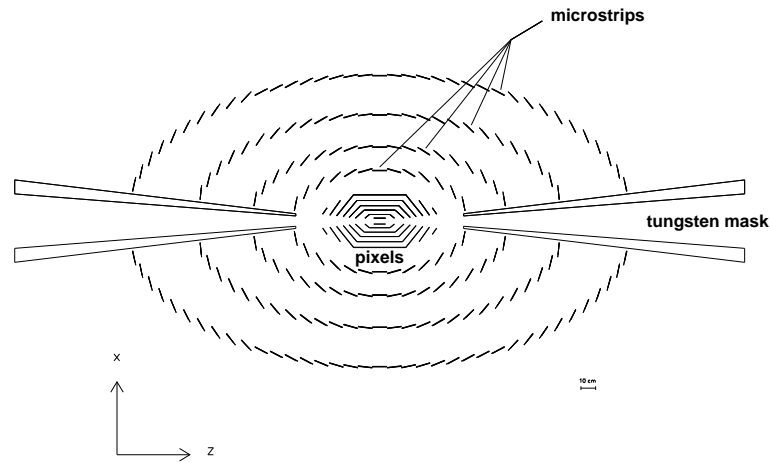


Figure 1: The all-silicon central tracker design. The tracker has a diameter of 2.0 metres and a length of 3.4 metres. The tiles in the outermost shell represent 3 layers of microstrip detectors in U-V-X configuration. In the 3 shells near mid-radius the tiles represent back-to-back microstrip detectors in small angle stereo configuration. The 6 vertexing layers consist of pixel detectors. The conical sections of the tungsten radiation masks are also shown.

All-Solid State Central Tracker: Cut-Away View

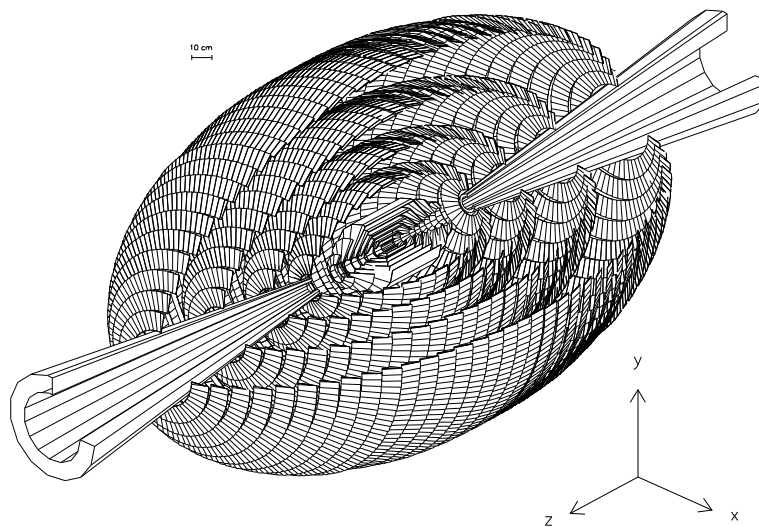


Figure 2: A 3-dimensional cut-away view of the central tracker and tungsten radiation masks.

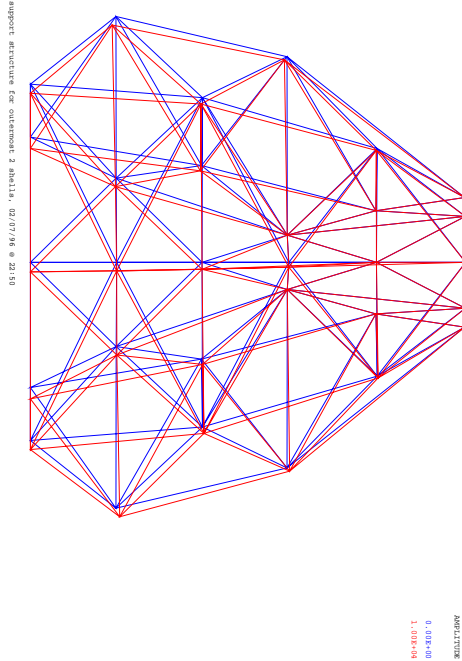


Figure 3: An example design for the large 3-dimensional mechanical support module that was used for finite analysis stress studies. Half of the module is shown, viewed from a position horizontally displaced from the IP in a direction perpendicular to the beam-line. The IP is half-way up the left hand side of the figure, with the unseen half of the module being the mirror image of the displayed half in a vertical plane through the IP. The two sets of slightly displaced lines show the structure a) without gravitational loading and b) with 10 000 times the deformation produced by gravitational loading.

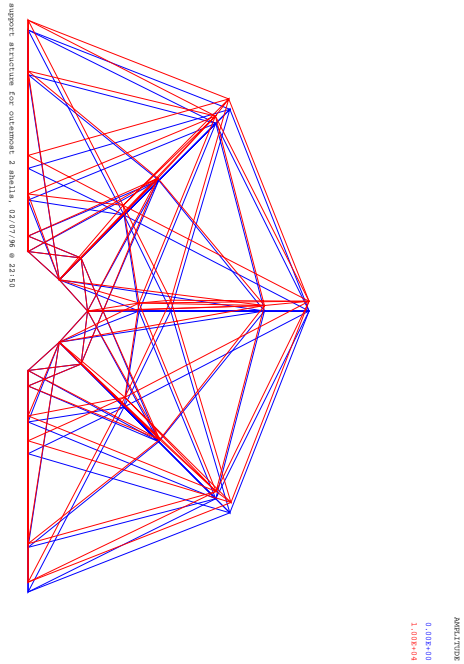


Figure 4: Same as figure 3, but in a view looking along the beam-pipe, such that the beam-pipe enters into the page half-way up the left hand side of the figure.

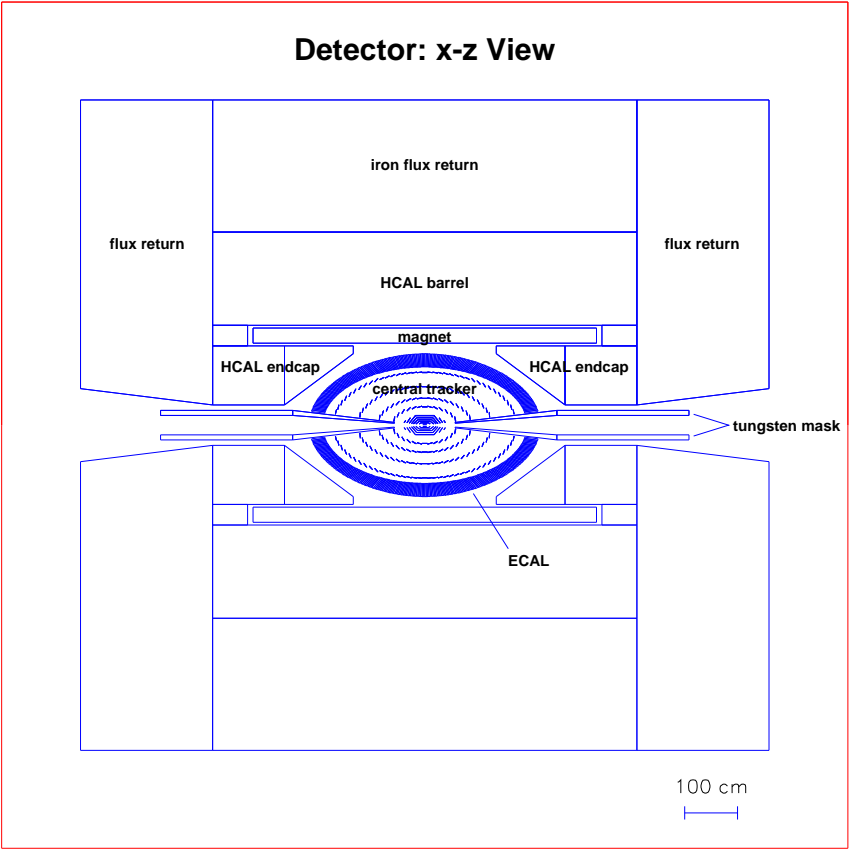


Figure 5: An example detector design which incorporates the all-silicon central tracker. The view is a cross-sectional slice along the beam-line.